journal homepage: www.intl.elsevierhealth.com/journals/cmpb

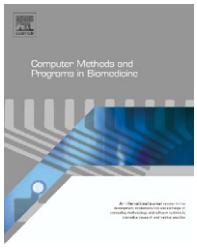

Computerized mouse pupil size measurement for pupillary light reflex analysis

Wei Lu[a], *Jinglu Tan*[a,*], *Keqing Zhang*[b,c], *Bo Lei*[b,c]

[a] *Department of Biological Engineering, University of Missouri, Columbia, MO 65211, USA*
[b] *Department of Veterinary Medicine & Surgery, University of Missouri, Columbia, MO 65211, USA*
[c] *Department of Ophthalmology, University of Missouri, Columbia, MO 65211, USA*

ARTICLE INFO

Article history:
Received 24 August 2007
Received in revised form
3 January 2008
Accepted 4 January 2008

Keywords:
Pupil size
Object detection
Image processing
Randomized Hough transform
Pupillary light reflex
Infrared

ABSTRACT

Accurate measurement of pupil size is essential for pupillary light reflex (PLR) analysis in clinical diagnosis and vision research. Low pupil–iris contrast, corneal reflection, artifacts and noises in infrared eye imaging pose challenges for automated pupil detection and measurement. This paper describes a computerized method for pupil detection or identification. After segmentation by a region-growing algorithm, pupils are detected by an iterative randomized Hough transform (IRHT) with an elliptical model. The IRHT iteratively suppresses the effects of extraneous structures and noise, yielding reliable measurements. Experimental results with 72 images showed a mean absolute difference of 3.84% between computerized and manual measurements. The inter-run variation for the computerized method (1.24%) was much smaller than the inter-observer variation for the manual method (7.45%), suggesting a higher level of consistency of the former. The computerized method could facilitate PLR analysis and other non-invasive functional tests that require pupil size measurements.

1. Introduction

Pupillary light reflex (PLR) has been employed in eye disease diagnosis and neurological research [1–8]. PLR requires accurate dynamic measurement of the pupil size (diameter or area) in response to stimulating light under infrared ambient illumination. Traditional measurement by direct observation is not quantitative and pupil diameter changes cannot be easily observed under dim lighting. Infrared imaging systems have been used to capture eye images in darkness for quantitative pupil size measurement [2,3,7–12]. The large quantity of image frames and usually high inter- and intra-observer variations necessitate an automated method for measuring pupil size. The key to such a method is to identify the pupil in an eye image. Pupil identification is also an important step for eye movement measurement, including ocular torsion [8,11,13–16].

The dark pupil in an eye image is usually identified either manually [3] or by a thresholding operation. In a thresholding-based method, pixels below a certain threshold value are classified as pupil pixels [8–15,17]. The pupil center coordinates are then computed as the center-of-mass of the pupil pixels [11,13,14], or determined by fitting a circle [8] or an ellipse [12] to the boundary points of the pupil. The effectiveness of thresholding-based approaches depends on a high pupil–iris contrast. Small laboratory animals often have low pupil–iris contrast and thus a thresholding method may fail to delineate the pupil [7–9]. A "bright pupil" infrared imag-

* *Corresponding author at*: Department of Biological Engineering, 215 Agricultural Engineering Building, University of Missouri, Columbia, MO 65211, USA. Tel.: +1 573 882 7778; fax: +1 573 884 5650.
E-mail address: TanJ@missouri.edu (J. Tan).
0169-2607/$ – see front matter © 2008 Elsevier Ireland Ltd. All rights reserved.
doi:10.1016/j.cmpb.2008.01.002

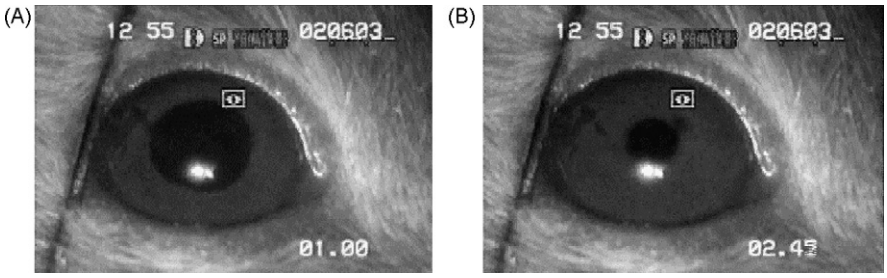

Fig. 1 – Two example mouse eye images: (A) an initial frame before light stimulation, and (B) a frame shortly after the first stimulating light pulse. The time stamp is shown in the bottom-right corner.

ing technique was found to improve the pupil–iris contrast in rabbits, but it required special illumination and collection optics [9]. Furthermore, large errors may occur for eye images containing artifacts, gaps and noises, which arise from eyelids, eyelashes, shadows, and corneal reflections of the light source [8,12,14]. To reduce these errors in thresholding-based methods, superfluous pupil boundary points were identified and excluded from circle fitting [8] or ellipse fitting [12]. In [8], an "interruption exclude algorithm" was used to exclude edge points whose radial distance values were beyond one standard deviation from the mean pupil radius. This algorithm is simple but may fail to exclude a potentially large number of non-pupil edge points [8]. In Ref. [12], four heuristics, based on observed curvature characteristics of the human pupil, were used to eliminate extraneous pupil boundary points. The challenge with this approach is to develop heuristics that are generally applicable.

This paper describes a method for pupil identification in infra-red mouse images based on a region-growing algorithm and an iterative randomized Hough transform (IRHT) [18]. Experimental tests showed that the method is effective and reliable.

2. Methods

2.1. *Experimental animals and image acquisition*

The experiments were conducted in accordance with the Association for Research in Vision and Ophthalmology (ARVO) Statement for the Use of Animals in Ophthalmic and Vision Research and the protocols were approved by the Animal Care and Use Committee (ACUC) of the University of Missouri, Columbia. Six 8-week-old C57BL/6 wild-type mice and six age-matched mice with retinal degeneration (RD) were used in this research (Jackson Laboratory, Bar Harbor, ME). Retinal degeneration is known to reduce eye responses to light stimulation as indicated by electroretinogram [19,20] and PLR [7]. The mice were kept in darkness for 12 h prior to experiments and were prepared under dim red light. During experiments, the animals were sedated with a mixture of xylazine (10 mg/kg i.m.) and ketamine (50 mg/kg i.m.). The body temperature of the mice was kept between 37 and 38 °C.

Pupil light reflexes were recorded in a dark room (0 lx). Ganzfeld white-light pulses of 10-μs duration were generated with a Grass PS22 Xenon visual stimulator (Grass Instrument Inc. West Warwick, RI). The maximum stimulating light intensity was 0.65 log cd s/m^2 and attenuated with neutral density filters. The luminance was calibrated with an IL-1700 radiometer/photometer (International Light, Newburyport, MA). The flashes were controlled with a UNIBLITZ shutter drive (VMM-T1, Vincent Associates, Rochester, NY) and the stimulus profile was evaluated with a phototransistor.

The mouse eye was imaged with a CCD video camera (Super HAD, Sony, New York, NY) under infrared illumination. A video stopwatch (VS-50, Horita, Mission Viejo, CA) was used to trigger the shutter diver and to start the timing. Video images of the pupil overlaid with timing were recorded with a VCR (SLVN500, Sony, New York, NY) at 30 frames per second. The recorded video was then digitized with a video grabber (Videum 1000 Plus, Winnov, Sunnyvale, CA) into uncompressed three-channel TIFF images of 320 × 240 pixels. The second (green) channel was found to provide the highest pupil–iris contrast and was saved as a monochromatic image for further analysis. Two example mouse eye images are shown in Fig. 1.

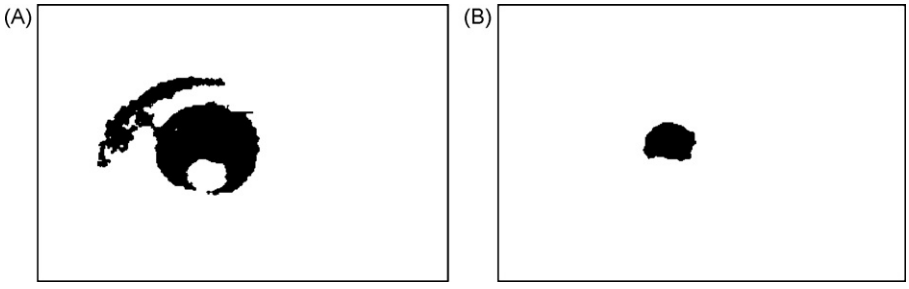

Fig. 2 – Results of the region-growing algorithm: (A) Segmented "pupil region" for Fig. 1A, and (B) segmented "pupil region" for Fig. 1B.

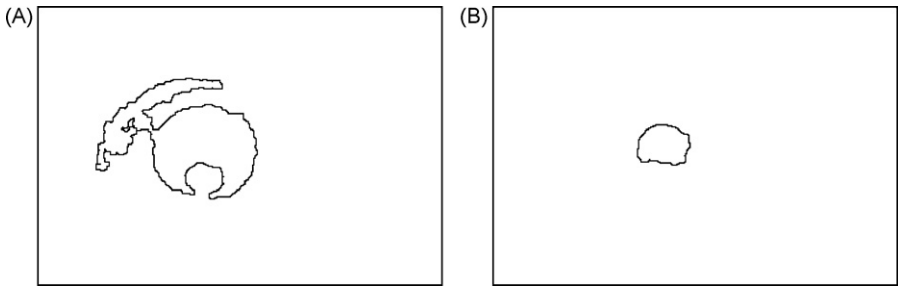

Fig. 3 – Extracted "pupil boundary" for (A) Fig. 2A, and (B) Fig. 2B.

2.2. *Pupil segmentation by region-growing*

The mouse pupil appears as a dark region inside the brighter iris (Fig. 1). The bright corneal reflections may be in the pupil (Fig. 1A), in the iris (not shown) or on the pupil–iris boundary (Fig. 1B). Because of the inherent low pupil–iris contrast and the poor quality of infrared mouse eye images, pupil segmentation by thresholding is often unreliable. In this work, a region-growing algorithm [21] was used for pupil segmentation. A "pupil region" was identified by successively appending neighboring pixels with similar gray levels to a seed point belonging to the pupil (Fig. 2). An automatic seed-selection method based on thresholding and center of mass was found unreliable. Instead, a seed point was manually selected near the pupil center in one arbitrary frame and used for all other frames (~1000) from the same imaging session. A 3×3 median filter was employed before region-growing to reduce noise. Corneal reflections and noise may cause holes in the grown region. A morphological hole-filling operation was therefore applied to fill these holes. The boundary of the "pupil region" was then smoothed by a morphological opening operation with a 1×1 structuring element. Finally, the "pupil boundary" was extracted by subtracting the "pupil region" image from the morphologically dilated (with a 1×1 structuring element) image (Fig. 3). Details of these operations can be found in Gonzalez and Woods [21] or other image processing textbooks.

2.3. *Pupil detection by iterative randomized Hough transform*

Corneal reflections of light sources, artifacts, discontinuities and noise are often observed in eye images [8,12,14]. Furthermore, the pupil–iris contrast is much lower and the image quality is relatively poorer in mouse eye images than in human eye images [7–9]. The region-growing algorithm alone is not sufficient for pupil identification. As shown in Fig. 3, the segmented "pupil boundary" did not contain a complete pupil border and yet included extraneous structures. Rather than excluding extraneous boundary points based on some heuristic radial distance [8] or curvature values [12], a new method named the iterative randomized Hough transform was used for pupil detection. The IRHT was recently developed for detection of incomplete ellipses in images with strong noise [18] and has been successfully applied to fetal head detection in clinical ultrasound images [22]. It applies a randomized Hough transform (RHT) to a region of interest in the image space with iterative parameter adjustments and reciprocating use of the image space and parameter space. The details of the IRHT can be found in [18] and only a brief description is given here.

Let $f(\mathbf{c}, \mathbf{z}) = 0$ represent a parametric curve in a binary image, where $\mathbf{c} = [\alpha_1, \ldots, \alpha_n]^t$ comprises n parameters and $\mathbf{z} = (x, y)$ represents the coordinates of a pixel with binary value 1. The pupil was modeled as an ellipse (for which $n = 5$) with the following stable and parametrically linear model [18,23,24]:

$$x^2 + y^2 - U(x^2 - y^2) - V2xy - Rx - Sy - T = 0 \quad (1)$$

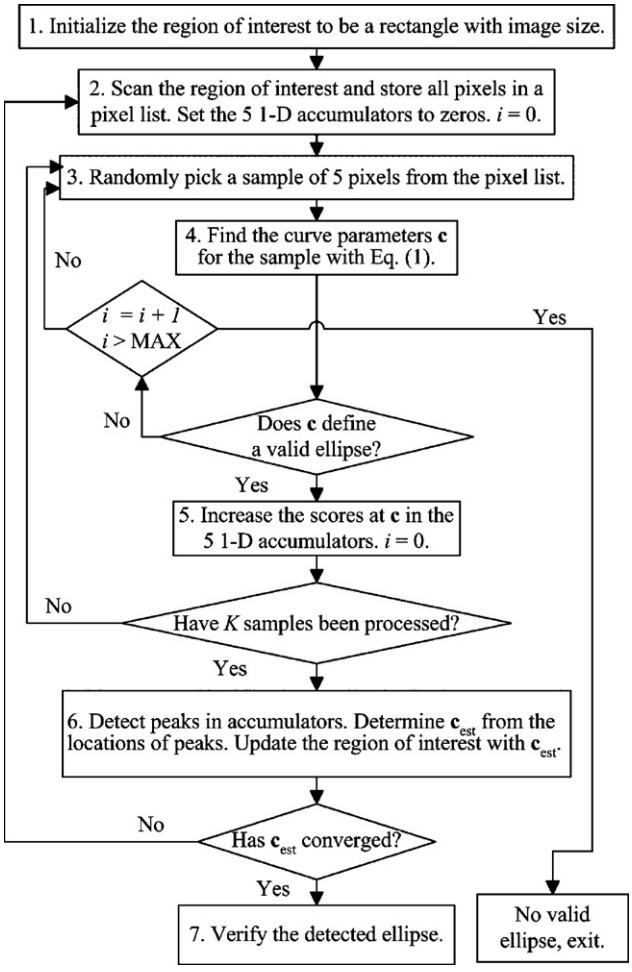

Fig. 4 – Flow diagram of the iterative randomized Hough transform for ellipse detection.

where $[U, V, R, S, T]^t$ comprises the five parameters. These parameters can be converted into the conventional parameters of an ellipse $c = [x_0, y_0, a, b, \phi]^t$, where (x_0, y_0) are the center coordinates, a and b are the major and minor semi-axes, and ϕ is the angle of rotation. While the pupil is often modeled and measured as a circle [8], it has been reported that an ellipse model is more accurate because the pupil boundary is elliptical when the eye is in eccentric positions [12,25]. In this study, manual measurements suggested that the imaged mouse pupils had an elongation ($e = b/a$) value close to but usually below unity. This supported the use of an elliptical model.

A flow diagram of the IRHT algorithm is shown in Fig. 4 for ellipse detection. In step 1, a region of interest, defined as the region in which the target ellipse is likely to lie, is initialized with the entire image. In step 2, the algorithm scans the region of interest and stores all foreground pixels in a pixel list and five 1D accumulators are initialized with zeros. In steps 3–4, a sample of five pixels is randomly picked from the pixel list, and a parameter solution c ($[x_0, y_0, a, b, \phi]^t$) is found for this sample by using Eq. (1). To ensure that c represents a valid ellipse, the following conditions need to be met: x_0, y_0, a, and b are positive; x_0 and y_0 are not larger than the image width and height, respectively; and a and b are not longer than one half of the diagonal of the image. If c is valid, the counts corresponding to c are increased by one in the five 1D accumulators; otherwise, c is discarded and a new sample is drawn. This random sampling and count accumulation process (steps 3–5) is repeated until K valid samples are processed. In the unlikely event that no valid **c** is found for a given large number of samples (MAX), the program exits and reports failure to detect an ellipse. In step 6, a parameter estimate, c_{est}, is determined from the locations of the count peaks in the 1D accumulators. c_{est} corresponds to the most likely ellipse estimated from the pixels within the current region of interest. The region of interest is then updated with an area constructed from the current parameter estimates. If the change in c_{est} from the previous iteration is small, the algorithm is considered to have converged; otherwise, steps 2–6 are repeated in the new region of interest. Moreover, since mouse pupils are known to have a high elongation, an elongation constraint of $e \geq 0.90$ was used to delineate the estimates further and to expedite the iteration process. If the IRHT converged in 10 iterations, it was considered successful, indicating that a dominant ellipse was identified, and the pupil area was then calculated as the ellipse area.

2.4. *Comparison of computerized and manual PLR measurements*

Seventy-two eye images were collected during a PLR experiment for a wild-type mouse. The images were obtained by taking every 10th frame in a video of 24 s (720 frames). A program was developed in Visual C++ (Microsoft, Redmond, WA) to capture video, process eye images (segmentation and detection), and provide a user interface. An Aphelion C++ library (AAI, Amherst, MA) was used for standard image processing operations.

To assess the accuracy of the computerized measurements and to analyze the inter-observer and inter-run variations, seven trained evaluators measured the pupil size in all images by manually fitting an ellipse to the perceived pupil boundary in Adobe Photoshop (Adobe, San Jose, CA). Since the IRHT involves random sampling of pixels, the computerized measurements may vary slightly from run to run. The IRHT-based pupil detection program was thus run seven times on each pupil boundary image to generate seven sets of computerized measurements. The seven sets of manual measurements were averaged to provide an average manual pupil size while the seven sets of computerized measurements were averaged to give an average computerized pupil size. The mean absolute difference, mean signed difference and correlation coefficient between the two types of measurement were calculated. The inter-observer and inter-run variations were computed as follows [26]:

$$\text{Inter-observer (or inter-run) variation} = \left[N\left(\frac{Q}{2}\right)\right]^{-1} \sum_{i=1}^{N} \sum_{p<q} \left| \frac{x_{pi} - x_{qi}}{x_{qi}} \right| \times 100 \quad (2)$$

where x_{ki} ($k = p$ or q) is the measurement of the ith image by the kth observer (or run), N the number of images and Q the number of observers (or runs), $\sum_{p<q}$ is the sum over all p and q such that $1 \leq p < q \leq Q$. Finally, the average computerized and manual pupil measurements were plotted against time to show the dynamic PLR response of measured pupil size to light stimulations.

3. Results

Fig. 2 shows two "pupil regions" resulting from the region-growing algorithm. The growing process stopped if the gray level difference between a new neighboring pixel and the average of all pixels already in the region exceeded a stopping threshold value (T) of 15. T was experimentally chosen based on the gray level contrast between the pupil region and the iris region, and on the uniformity of the pupil region. The upper limit of T was determined by the smallest contrast between the pupil and the iris regions, and the lower limit was determined by the largest variation inside the pupil region. For the image in Fig. 1A, the "pupil region" was grown too much into the iris region (Fig. 2A), which suggested that T should be lowered. For the image in Fig. 1B, however, the "pupil region" was not grown enough to include all pupil pixels (Fig. 2B), which suggested that T should be increased. The selection of T was therefore a compromise for all the images. In practice, the user may experimentally change this value. The extracted "pupil boundary" images are shown in Fig. 3. Holes from the reflection of light source, extraneous parts in the iris region, incomplete or corrupted boundaries, and rough edges are obvious in Figs. 2 and 3. The true pupil boundaries have yet to be identified.

The results of pupil detection by the IRHT are shown in Figs. 5 and 6. The IRHT took five and three iterations to converge for the two example cases, respectively. It is clear from Fig. 5 that non-pupil boundary pixels were gradually excluded from the region of interest and that the estimation progressively became close to the true pupil. The detected ellipses

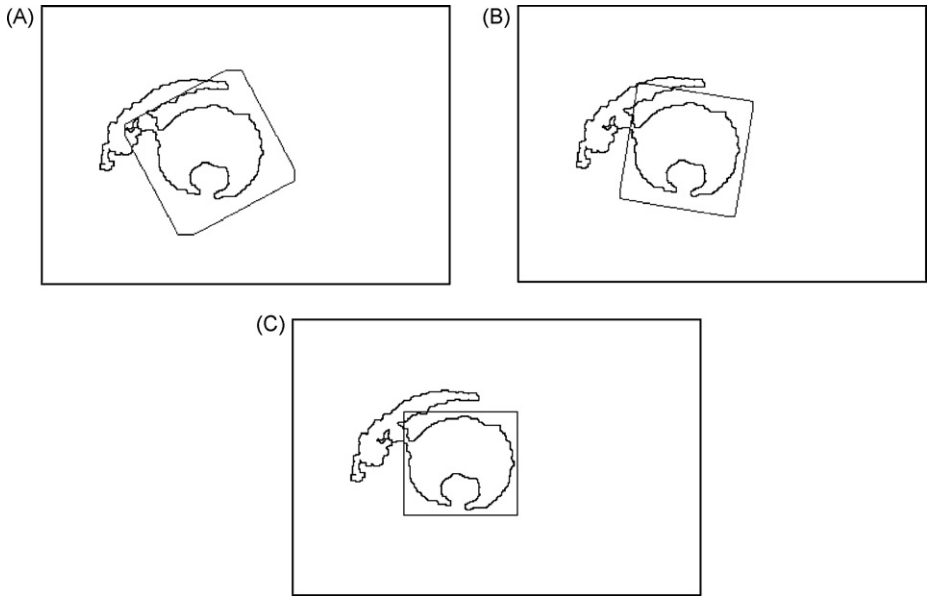

Fig. 5 – Pupil detection by the IRHT for Fig. 3A. The regions of interest are displayed as gray octagons or rectangles: (A) after the first iteration of the IRHT, the estimation is biased by extraneous structures in the iris, (B) after the third iteration, the angle of rotation is still incorrect and (C) after the fifth iteration, the IRHT has converged.

are superimposed as thick gray lines on the "pupil boundary" images (Fig. 6A and B) and on the original eye images (Fig. 6C and D). It is clear that the IRHT reliably and accurately detected the pupil boundaries in these two examples. The corneal reflections were either close to or on the pupil boundary, but they did not negatively affect the effectiveness of the algorithm. This was because the IRHT is a probability-based algorithm that has built-in capabilities to handle missing or superfluous boundary points and noise.

All the 72 images were processed in the same way seven times and all IRHT runs resulted in successful ellipse detections. The IRHT automatically gave the long and the short axes of the ellipses, which could be used as size measures if so desired. The ellipse area, however, is conventionally used as the measure of pupil size and was thus computed in this research. The measurements were in number of pixels. It is simple, however, to scale the measurements into values in real units since the pixel size can be easily determined by imaging a ruler or objects of known sizes. The area measurements were normalized as percentages of the first average manual measurement in this work because the relative size change, rather than the absolute size, is used in PLR analysis.

A scatter plot of the average computerized and manual measurements is shown in Fig. 7. The line of equality

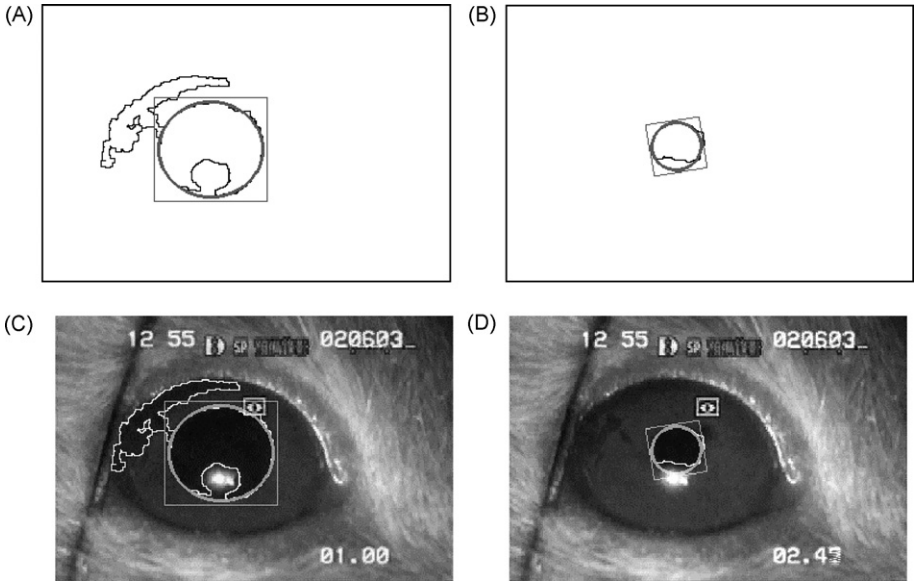

Fig. 6 – Results of pupil detection by the IRHT. The resulting ellipse is superimposed onto the "pupil boundary" images (A and B) and the original eye images (C and D).

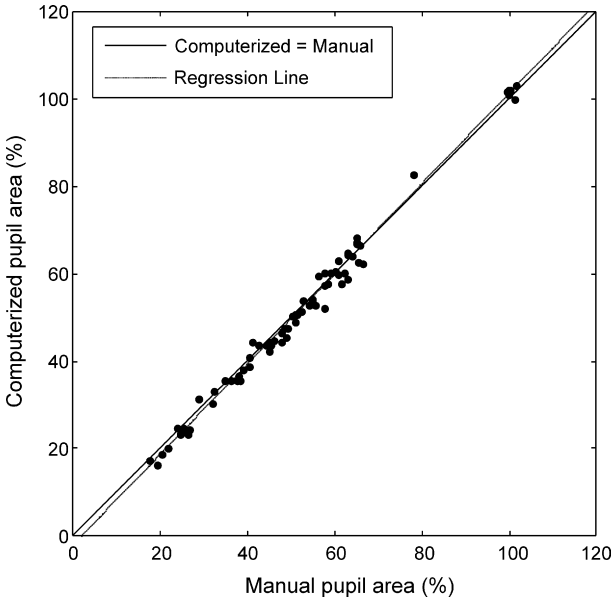

Fig. 7 – Scatter plot of the average computerized and the average manual pupil area measurements for 72 mouse eye images. The diagonal is the line of equality. Solid line: the line of equality. Dash-dot line: regression line representing computerized pupil area = 1.03 × manual pupil area – 2.29. Note that all data values normalized as percentage of the first average manual measurement.

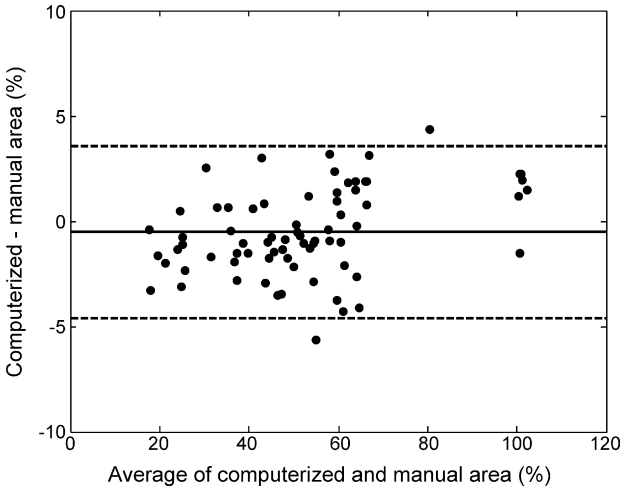

Fig. 8 – Bland-Altman plot of the computerized and the manual pupil area measurements (in percentage of the first average manual measurement). Solid line: the mean difference. Dashed lines: 95% limits.

and a linear regression line are also included in the figure. The correlation coefficient between the two types of measurement was 0.996. The slope of the regression line was 1.03 with a 95% confidence interval [1.01, 1.06], only slightly above the perfect unity. While the slope value hints a possible minor dependence of measurement difference on measurement magnitude, it indicates a practically excellent level of agreement between the two types of measurement.

To further confirm the agreement between the two methods, the commonly used Bland-Altman plot [27] is shown in Fig. 8 and the associated statistics presented in Table 1. The mean signed difference was −0.52% ($p = 0.03$), which means that, for the sample, the computerized measurements were only slightly below the manual measurements. The 95% limits of the difference were [−4.61%, 3.57%]. Seventy of the 72 measurements fell in this 95% limits (Fig. 8). There was no discernible trend or dependence of the difference on measurement magnitude. This again indicates a high level of agreement between the two methods. It should be noted that the minor difference is not necessarily an error of the automatic method. Examination of the data and images showed that the two points outside the 95% limits were due to inconsistencies in the manual measurements.

Table 1 – Agreement between automatic and manual pupil area measurements[a]

Measurement	Pupil area
No. of images	72
Mean signed difference (%[b])	−0.52 (2.05)
p value for t-test	0.03
Mean absolute difference (%[b])	1.77 (1.14)
95% limits of agreement (%[b])	[−4.61, 3.57]

[a] Values in parentheses are standard deviations.
[b] Percentage of the first average manual measurement.

The inter-observer variation was 7.45% and the inter-run variation was much smaller at 1.24%. The standard deviation of the seven manual measurements averaged for all 72 images was 2.79%, while that of the seven computerized measurements was 0.79%. These statistics suggest that the computerized measurements were more consistent than the manual measurements. The difference between the computerized and the manual measurements was smaller than the inter-observer variation.

The computerized and the manual measurements were plotted against time in Fig. 9, showing the pupil size responses of a subject to two stimulating light pulses. The two curves agreed with each other closely for the testing period. The persistent random fluctuations in pupil size were supposedly due to random firing of Edinger–Westphal nucleus cells and have been found to be an indicator of narcolepsy [5]. Very similar results were obtained for the other normal or RD subjects. For the normal subjects, significant responses to all four levels of stimulating light were observable in PLR. As expected, the PLR amplitudes increased with the intensity of stimulation. Compared with the normal subjects, the threshold for pupillary response in the RD subjects increased for more than 2 log units and the maximum amplitude decreased by approximately 40% at 0.65 log cd s/m^2. Similar PLR results were reported for another mouse model of retinal degeneration (*Rpe65*$^{-/-}$) and normal mice by Aleman et al. [7].

The computerized pupil segmentation and detection method has been implemented on a 2.4-GHz Pentium-IV PC

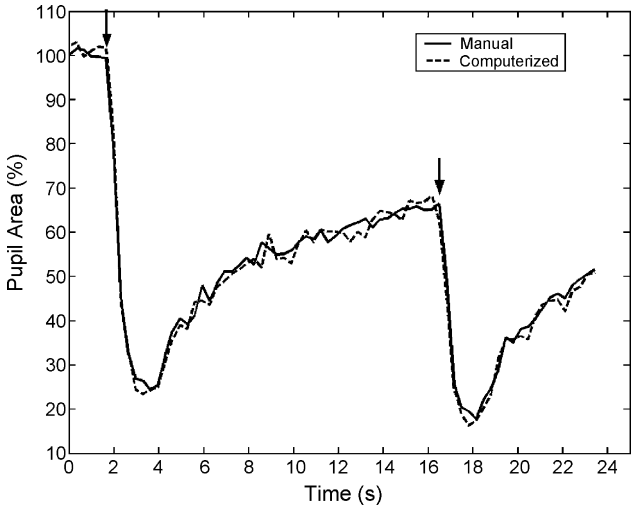

Fig. 9 – Computerized and manual measurements of pupil size response to stimulating light pulses. Arrows indicate the onset of a 10-μS flash light.

for routine PLR analysis. The system takes an average time of 0.9 s to process each image. This includes times for reading and writing images, segmenting and detecting the pupil, and outputting the results.

4. Discussion

Image blurring, matched filtering and other image processing operations were used to locate and remove the holes in the pupil caused by corneal reflections in Ref. [14]. If the corneal reflection falls on the pupil boundary, however, the accuracy of the procedure degrades. Further, the size of the corneal reflection was assumed to be a known constant. The method reported here does not rely on any assumed size or location of corneal reflections for accurate detection of the pupil boundary.

The algorithm allows for user input and intervention. For the region-growing algorithm, a seed point needs to be selected on an arbitrary frame of an imaging session. In the PLR study, a single seed point was found to be sufficient for all frames in the same session. If the pupil center moves significantly, for example, in eye-tracking experiments, the seed point may be adaptively changed to be the pupil center determined by the IRHT for the previous frame. The user still needs to select only the first seed point. Moreover, the user has the options to adjust the stopping threshold value T for the region-growing algorithm and the number of samples (K) for the IRHT algorithm. The effects of T and its selection procedure have been discussed in the last section. The selection the K value is not so critical so long as it is large enough to give sufficient entries for the parameter histograms. In this study, a K of 100 was found adequate and K values greater than 100 did not change the results significantly. A larger K may help when more noise is present in the images. A detailed analysis can be found in [18] on the robustness of the IRHT algorithm for different noise types and levels and the probability of failure as a function of sample size.

5. Conclusion

The method developed was found reliable and efficient for pupil detection and measurement in infrared mouse eye images. The computerized measurements were in good agreement with and were more consistent than manual measurements. This method provides a practical and objective way for measuring pupil size. It has great potential as an important tool in neurological research and eye disease diagnosis.

Conflict of interest

None.

Acknowledgements

This research was supported in part by a Prevent Blindness America/Fight for Sight Grant-in-aid (GA02044, BL) and the University of Missouri Flo-Dickey Funk research fellowship (WL). The authors thank the colleagues in the Bioinstrumentation Lab at University of Missouri, Columbia for assisting with the data collection.

REFERENCES

[1] R.J. Lucas, R.H. Douglas, R.G. Foster, Characterization of an ocular photopigment capable of driving pupillary constriction in mice, Nat. Neurosci. 4 (2001) 621–626.
[2] R.J. Lucas, S. Hattar, M. Takao, D.M. Berson, R.G. Foster, K.W. Yau, Diminished pupillary light reflex at high irradiances in melanopsin-knockout mice, Science 299 (2003) 245–247.
[3] M.E. Pennesi, A.L. Lyubarsky, E.N. Pugh Jr., Extreme responsiveness of the pupil of the dark-adapted mouse to steady retinal illumination, Invest. Ophthalmol. Vis. Sci. 39 (1998) 2148–2156.
[4] W.D. O'Neill, K.P. Trick, The narcoleptic cognitive pupillary response, IEEE Trans. Biomed. Eng. 48 (2001) 963–968.
[5] W.D. O'Neill, A.M. Oroujeh, S.L. Merritt, Pupil noise is a discriminator between narcoleptics and controls, IEEE Trans Biomed. Eng. 45 (1998) 314–322.
[6] R.N. Van Gelder, R. Wee, J.A. Lee, D.C. Tu, Reduced pupillary light responses in mice lacking cryptochromes, Science 299 (2003) 222.
[7] T.S. Aleman, S.G. Jacobson, J.D. Chico, M.L. Scott, A.Y. Cheung, E.A. Windsor, M. Furushima, T.M. Redmond, J. Bennett, K. Palczewski, A.V. Cideciyan, Impairment of the transient pupillary light reflex in rpe65(−/−) mice and humans with leber congenital amaurosis, Invest. Ophthalmol. Vis. Sci. 45 (2004) 1259–1271.
[8] T. Sakatani, T. Isa, Pc-based high-speed video-oculography for measuring rapid eye movements in mice, Neurosci. Res. 49 (2004) 123–131.
[9] R.B. Murray, M.H. Loughnane, Infrared video pupillometry: a method used to measure the pupillary effects of drugs in small laboratory animals in real time, J. Neurosci. Methods 3 (1981) 365–375.
[10] A.H. Nguyen, L.W. Stark, Model control of image processing: pupillometry, Comput. Med. Imaging Graph 17 (1993) 21–33.
[11] S.T. Moore, I.S. Curthoys, S.G. McCoy, Vtm—an image-processing system for measuring ocular torsion, Comput. Methods Programs Biomed. 35 (1991) 219–230.

[12] D. Zhu, S.T. Moore, T. Raphan, Robust pupil center detection using a curvature algorithm, Comput. Methods Programs Biomed. 59 (1999) 145–157.
[13] A.H. Clarke, W. Teiwes, H. Scherer, Video-oculography—an alternative method for measurement of three-dimensional eye movements, in: R. Schmid, D. Zambarbieri (Eds.), Oculomotor Control and Cognitive Processes, Elsevier, New York, NY, 1991.
[14] J.B. Mulligan, Image processing for improved eye-tracking accuracy, Behav. Res. Methods Instrum. Comput. 29 (1997) 54–65.
[15] E. Groen, J.E. Bos, P.F. Nacken, B. de Graaf, Determination of ocular torsion by means of automatic pattern recognition, IEEE Trans. Biomed. Eng. 43 (1996) 471–479.
[16] D. Zhu, S.T. Moore, T. Raphan, Robust and real-time torsional eye position calculation using a template-matching technique, Comput. Methods Programs Biomed. 74 (2004) 201–209.
[17] M. Wingate, B. Hood, H. Shi, P. Phan, Automated pupil size determination for evaluating fluctuations in physiological arousal, in: Proceedings of the ICSP' 98, 1998.
[18] W. Lu, J. Tan, Detection of incomplete ellipse in images with strong noise by iterative randomized Hough transform (IRHT), Pattern Recogn. 41 (2008) 1268–1279.
[19] C. Zhang, B. Lei, T.T. Lam, F. Yang, D. Sinha, M.O. Tso, Neuroprotection of photoreceptors by minocycline in light-induced retinal degeneration, Invest. Ophthalmol. Vis. Sci. 45 (2004) 2753–2759.
[20] B. Lei, The erg of guinea pig (cavis porcellus): comparison with i-type monkey and e-type rat, Doc. Ophthalmol. 106 (2003) 243–249.
[21] R.C. Gonzalez, R.E. Woods, Digital Image Processing, Addison-Wesley, Reading, MA, 1992.
[22] W. Lu, J. Tan, R. Floyd, Automated fetal head detection and measurement in ultrasound images by iterative randomized Hough transform, Ultrasound Med. Biol. 31 (2005) 929–936.
[23] V.F. Leavers, The dynamic generalized Hough transform: its relationship to the probabilistic Hough transforms and an application to the concurrent detection of circles and ellipses, Computer Vision Graph. Image Process.: Image Und. 56 (1992) 381–398.
[24] A.B. Forbes, Fitting an Ellipse to Data Technical Report DITC 95/87, National Physical Laboratory, Teddington, UK, 1987.
[25] K. Matsuda, T. Nagami, All purpose measurement system of the eye positions, in: Proceedings of the 12th Symposium on Biological and Physiological Engineering, Machida, Japan, 1998.
[26] R.L. Deter, R.B. Harrist, F.P. Hadlock, R.J. Carpenter, Fetal head and abdominal circumferences. I. Evaluation of measurement errors, J. Clin. Ultrasound 10 (1982) 357–363.
[27] J.M. Bland, D.G. Altman, Measuring agreement in method comparison studies, Stat. Methods Med. Res. 8 (1999) 135–160.